Progress In Electromagnetics Research C, Vol. 164, 214–223, 2026

(Received 30 November 2025, Accepted 24 December 2025, Scheduled 12 January 2026)

ADMM-Based Sparse SAR Imaging Algorithm with Cholesky Decomposition and Dual-Momentum Coupling

Encheng Wang[1], Xuechen Zhang[1,*], Daming Lin[2], and Shumao Qiu[2]

[1] *North China University of Technology, China*
[2] *Research Institute of Highway, Ministry of Transport, China*

ABSTRACT: To address the challenges of high computational complexity in linear system solving and slow convergence of the Alternating Direction Method of Multipliers (ADMM) for compressed sensing Synthetic Aperture Radar (SAR) imaging, this study proposes a precomputation strategy based on Cholesky decomposition. Specifically, the system matrix is decomposed once during the initialization phase and reused across subsequent iterations, substantially reducing the computational overhead associated with the primal variable update. Furthermore, a novel dual-momentum coupling mechanism is designed, and building on Nesterov extrapolation, this mechanism integrates cross-momentum interactions between the real and imaginary components of dual variables, along with the historical variation trends of primal variables, thereby effectively accelerating overall convergence. Both simulated and measured data results demonstrate that the proposed method achieves a significant improvement in computational efficiency while ensuring high imaging quality.

1. INTRODUCTION

Synthetic Aperture Radar (SAR) is an active remote sensing imaging radar that enables all-time and all-weather Earth observation via penetrating microwaves and has wide applications in diverse fields such as marine development and military reconnaissance [1]. High resolution represents its development trend, as it can enhance the capability of target monitoring and recognition. However, constrained by radar resolution theory and Nyquist sampling theorem, high resolution inevitably leads to enormous computational complexity and storage challenges, which restrict technological advancement [2].

To address the computational and storage challenges in high-resolution SAR imaging, researchers have introduced the Compressed Sensing (CS) theory, which can be sampled at a rate far below the Nyquist sampling frequency, and the echo signal can be reconstructed with high precision using only a small amount of observed data [3]. Compared with traditional pulse compression-based SAR imaging algorithms, CS-based sparse SAR imaging algorithms can achieve high-resolution imaging with merely a small quantity of echo data and exhibit stronger suppression capabilities for signal sidelobes and scene noise; even for full-sampling systems, sparse signal processing still contributes to improving reconstruction performance [4].

In sparse signal reconstruction, L_1 regularization has been widely applied in fields such as compressed sensing and radar imaging because of its effectiveness in promoting solution sparsity [5]. However, in practical applications, L_1 regularization tends to overpenalize large coefficients, which result in the underestimation of the amplitude of strong scatterers, thus degrading the reconstruction accuracy [6, 7]. To mitigate this issue, some studies have adopted non-convex regularization terms as alternatives. Specifically, Ref. [8] introduced $L_{1/2}$ regularization into sparse SAR imaging and combined it with an iterative half-thresholding algorithm, achieving a linear convergence rate under specific conditions. Although such methods can significantly enhance the point target features, the continuity of regional targets is equally crucial in tasks such as image segmentation.

To preserve the smooth characteristics of targets within regions, researchers have introduced the Total Variation (TV) norm as a regularization term to constrain the variation amplitude between adjacent pixels, thereby maintaining the spatial continuity of backscattering coefficients in the region [9]. However, in complex scenarios, it is often necessary to simultaneously achieve high-resolution focusing of point targets and structural integrity of regional targets, which is difficult for a single regularization model to balance. Therefore, composite regularization methods have emerged, among which joint L_1-TV regularization has become a mainstream choice owing to its practicality and effectiveness [10, 11].

However, composite regularization models typically involve multiple variables and constraints, leading to a significant increase in the difficulty of solving joint minimization problems. Similarly, inverse scattering problems in other wave phenomena — specifically elastic waves and acoustic waves — also face the ill-posedness and computational bottlenecks of high-resolution imaging. For instance, the corner analysis of nonradiating elastic sources in inhomogeneous media [12], the corner detection of dislocations in elastic bodies [13], the coupled-physics transmission eigenvalue problem [14], and the quasi-Minnaert resonances in high-contrast acoustic structures [15] all involve handling non-smooth terms and accelerating convergence through regularization frameworks to achieve unique

---

* Corresponding author: Xuechen Zhang (3167053462@qq.com).

doi:10.2528/PIERC25113001

identifiability and an efficient solution. The Alternating Direction Method of Multipliers (ADMM) has become a commonly used tool for solving such problems because of its excellent decomposition capability and convergence performance [16]. By introducing auxiliary variables, which decompose the original problem into a series of easily solvable subproblems and gradually approximates the optimal solution through alternating updates of the primal variables, auxiliary variables, and dual variables. Owing to its modular structure and stable convergence characteristics, ADMM has been widely applied in various fields, including signal processing [17], image restoration [18], speech recognition [19], deep learning [20], and electronic countermeasures [21].

Despite the favorable theoretical properties of the ADMM, its computational efficiency bottleneck remains prominent, primarily focusing on solving the large-scale linear system in the primal variable update (x-update) step. For high-resolution imaging tasks, the coefficient matrix $\mathbf{M} \in R^{N\times N}$ of this linear system often reaches a dimension N of the order of hundreds of thousands or even millions. If direct solvers such as Lower-Upper (LU) decomposition [22] or Gaussian elimination [23] are adopted, the computational complexity of a single iteration is as high as $O(N^3)$, which makes it difficult to meet the real-time requirements. Even when switching to iterative solvers, such as the Conjugate Gradient (CG) method, slow convergence may still occur because of the potentially large condition number of the system matrix, which requires a large number of inner iterations to achieve the desired accuracy, resulting in a significant overall computational cost.

In particular, in complex domain imaging problems (e.g., SAR and Magnetic Resonance Imaging (MRI)), the observed signals are inherently complex. Conventional processing methods require splitting unknown variables into real and imaginary parts for joint modeling, expanding the problem dimension from N to $2N$, thus increasing the size of the corresponding linear system to $2N \times 2N$. In this case, the computational burden of both the direct and iterative methods grows geometrically, severely limiting the practicality of the algorithm. Even if the Kronecker structure is used to preserve sparsity, the computation of the linear system remains the core bottleneck that restricts the real-time performance of the algorithm. Therefore, there is an urgent need to develop efficient numerical acceleration strategies that significantly reduce computational costs while ensuring reconstruction accuracy.

To address the aforementioned issues, this paper proposes an efficient ADMM acceleration framework for complex-valued SAR imaging. The core of this framework lies in two synergistically designed key mechanisms.

On one hand, leveraging the Hermitian Positive Definite (HPD) structure of the coefficient matrix in the x-update subproblem, Cholesky decomposition [24] is preperformed during the algorithm initialization phase to achieve "one-time decomposition, multiple reuses". Subsequent iterations only require low-complexity forward-backward substitution operations, significantly reducing computational overhead. Compared with general decomposition methods such as LU or Orthogonal–Triangular (QR), Cholesky decomposition eliminates the need for pivoting, only requires storing the lower triangular factor, and can directly handle complex-valued variables. This avoids the dimension doubling caused by splitting complex signals into real and imaginary parts, thereby substantially saving memory and computational load while ensuring numerical stability.

On the other hand, aiming at the limitation of the traditional Nesterov extrapolation momentum acceleration method — where Nesterov extrapolation is only applicable to real-valued sequences and difficult to characterize the intrinsic structure of complex-domain variables — a novel dual-momentum coupling mechanism is designed. It not only introduces Nesterov-type extrapolation for dual variables to accelerate their convergence, but also constructs a cross-momentum interaction structure between their real and imaginary parts, while integrating the historical variation trend of primal variables to form a composite inertial driving mode. This mechanism explicitly models the strong physical correlation between the real and imaginary parts of SAR complex reflectivity, which not only effectively reduces the number of required iterations but also better maintains the physical consistency in phase-sensitive imaging.

The above two mechanisms are organically integrated, significantly improving the overall efficiency and reconstruction quality of sparse SAR imaging in the complex domain without compromising the convergence guarantee of ADMM.

2. SPARSE SAR IMAGING MODEL

In SAR imaging, the introduction of sparse signal processing theory has led to the development of sparse SAR imaging methods that can overcome the limitations of the Nyquist sampling theorem, acquire data at a sampling rate far lower than that specified by the theorem, and achieve a high-precision reconstruction of the observed scene.

In the sparse SAR imaging model, the relationship between the echo sampled data $\mathbf{Y} \in \mathbb{C}^{P\times Q}$ and scene $\mathbf{X} \in \mathbb{C}^{M\times N}$ is given as follows:

$$\mathbf{y} = \Phi\mathbf{x} + \mathbf{n} \tag{1}$$

where $\mathbf{y} \in \mathbb{C}^{L\times 1}$ denotes the echo sampled data formed by stacking each column of $\mathbf{Y}$ into a column vector, with $L = P \times Q$; $\mathbf{x} \in \mathbb{C}^{K\times 1}$ is the column vector obtained by stacking each column of the observed scene $\mathbf{X}$; $K = M \times N > L$; $\Phi \in \mathbb{C}^{L\times K}$ represents the measurement matrix; and $\mathbf{n} \in \mathbb{C}^{K\times 1}$ is the noise vector.

Sparse SAR target scenes typically consist of discrete point targets and continuously distributed regional targets. To preserve both types of features simultaneously, a composite optimization model with joint L_1-TV regularization was adopted, which is expressed as follows:

$$\min_{\mathbf{x}\in\mathbb{C}^{K\times 1}} \frac{1}{2}\|\Phi\mathbf{x} - \mathbf{y}\|_2^2 + \lambda_1\|\mathbf{x}\|_1 + \lambda_2\|\mathbf{D}\mathbf{x}\|_1 \tag{2}$$

where $\mathbf{D}$ denotes the first-order difference operator, which is used to extract image gradient information; λ_1 and λ_2 are regularization weight parameters that balance the data fidelity term, sparsity constraint, and the smoothness constraint, respectively.

Specifically, the first term ensures the consistency between the reconstructed result and the observed data; the second term promotes the sparse representation of point targets; and the third term maintains the continuity of pixels within regions through TV constraint, suppresses noise, and enhances edge structures.

Owing to the non-differentiability of the objective function and the presence of multiple non-smooth terms, direct optimization is challenging. The ADMM method transforms this non-separable problem into a more tractable form by introducing auxiliary variables. Specifically, we introduce $\mathbf{z} = \mathbf{x}$ to handle the L_1 regularization term, and $\mathbf{v} = \mathbf{D}\mathbf{x}$ to address the TV regularization term. Thus, the equivalent constrained optimization problem is obtained as follows:

$$\min_{\mathbf{x}\in\mathbb{C}^{K\times 1}} \frac{1}{2}\|\Phi\mathbf{x}-\mathbf{y}\|_2^2 + \lambda_1\|\mathbf{z}\|_1 + \lambda_2\|\mathbf{v}\|_1 \tag{3}$$

The corresponding augmented Lagrangian function is given by:

$$\begin{aligned}\mathcal{L}_{\rho_1,\rho_2}(\mathbf{x},\mathbf{z},\mathbf{v};\mathbf{u}_1,\mathbf{u}_2) = &\frac{1}{2}\|\Phi\mathbf{x}-\mathbf{y}\|_2^2 + \lambda_1\|\mathbf{z}\|_1\\ &+\lambda_2\|\mathbf{v}\|_1 + \frac{\rho_1}{2}\|\mathbf{x}-\mathbf{z}+\mathbf{u}_1\|_2^2\\ &+\frac{\rho_2}{2}\|\mathbf{D}\mathbf{x}-\mathbf{v}+\mathbf{u}_2\|_2^2 \end{aligned}\tag{4}$$

where $\mathbf{u}_1, \mathbf{u}_2$ are scaled dual variables, and $\rho_1, \rho_2 > 0$ are penalty parameters. In all experiments, ρ_1 and ρ_2 are fixed to constant values to avoid introducing additional tuning complexity. The proposed algorithm converges stably for a wide range of ρ values, and the reconstruction performance is not sensitive to their exact settings. In this study, both ρ_1 and ρ_2 are set to 2.

3. ADMM-BASED ACCELERATION MECHANISM

3.1. ADMM Iterative Updates

The ADMM alternately minimizes the aforementioned augmented Lagrangian function to sequentially update the primal, auxiliary, and dual variables. The specific iterative steps are as follows:

$$\begin{aligned}\mathbf{x}^{k+1} &= \arg\min_{\mathbf{x}} \mathcal{L}(\cdot) \implies \left(\Phi^H\Phi + \rho_1\mathbf{I} + \rho_2\mathbf{D}^H\mathbf{D}\right)\mathbf{x}^{k+1}\\ &= \Phi^H\mathbf{y} + \rho_1\left(\mathbf{z}^k - \mathbf{u}_1^k\right) + \rho_2\mathbf{D}^H\left(\mathbf{v}^k - \mathbf{u}_2^k\right)\end{aligned}\tag{5}$$

Let $\mathbf{M}$ denote the system matrix:

$$\mathbf{M} = \Phi^H\Phi + \rho_1\mathbf{I} + \rho_2\mathbf{D}^H\mathbf{D} \tag{6}$$

Since $\Phi^H\Phi$ and D^HD are both Hermitian positive semi-definite matrices, the addition of the term $\rho_1 I$ (with $\rho_1 > 0$, which is strictly positive definite) ensures that the resulting system matrix M is strictly Hermitian positive definite (HPD). This HPD property guarantees the uniqueness of the solution to the corresponding optimization problem and provides a theoretical basis for the stable convergence of the iterative algorithm. where $\mathbf{b}^k$ denotes the right-hand side vector at the k-th iteration:

$$\mathbf{b}^k = \Phi^H\mathbf{y} + \rho_1\left(\mathbf{z}^k - \mathbf{u}_1^k\right) + \rho_2\mathbf{D}^H\left(\mathbf{v}^k - \mathbf{u}_2^k\right) \tag{7}$$

Thus, the $\mathbf{x}$-update step is equivalent to solving the linear system:

$$\mathbf{M}\mathbf{x}^{k+1} = \mathbf{b}^k \tag{8}$$

Second, the $\mathbf{z}$-update step is solved via the soft-thresholding operation:

$$\mathbf{z}^{k+1} = \mathcal{S}_{\lambda_1/\rho_1}\left(\mathbf{x}^{k+1} + \mathbf{u}_1^k\right) \tag{9}$$

Third, the $\mathbf{v}$-update step is solved via the TV soft-thresholding operation:

$$\mathbf{v}^{k+1} = \mathcal{S}_{\lambda_2/\rho_2}\left(\mathbf{D}\mathbf{x}^{k+1} + \mathbf{u}_2^k\right) \tag{10}$$

Fourth, the dual variables are updated as follows:

$$\mathbf{u}_1^{k+1} = \mathbf{u}_1^k + \mathbf{x}^{k+1} - \mathbf{z}^{k+1} \tag{11}$$

$$\mathbf{u}_2^{k+1} = \mathbf{u}_2^k + \mathbf{D}\mathbf{x}^{k+1} - \mathbf{v}^{k+1} \tag{12}$$

where the updates follow the complementary slackness condition of ADMM, which adjusts the dual variables based on the residual of the primal-auxiliary variable constraints to promote iteration convergence.

3.2. Matrix Precomputation Based on Cholesky Decomposition

The system matrix $\mathbf{M}$ has special structural properties: $\Phi^H\Phi$ reflects the geometric characteristics of the observation process and is usually positive semi-definite. The identity matrix term $\rho_1\mathbf{I}$ provides a regularization effect, and $\rho_2\mathbf{D}^H\mathbf{D}$ is the Gram matrix of the difference operator, which corresponds to a form of the discrete Laplacian operator. Overall, $\mathbf{M}$ is a Hermitian positive definite (HPD) matrix, which provides an important theoretical foundation for subsequent numerical optimization; thus, we can perform a one-time matrix decomposition on $\mathbf{M}$ before the algorithm starts, and then reuse the decomposition result in each iteration to quickly solve the linear system, significantly reducing the computational complexity of the $\mathbf{x}$-update step.

Given that $\mathbf{M}$ is a Hermitian positive definite matrix, Cholesky decomposition is the most natural and efficient choice and factorizes $\mathbf{M}$ into the form $\mathbf{M} = \mathbf{L}\mathbf{L}^H$, where $\mathbf{L}$ is a lower triangular matrix with positive real diagonal entries. This decomposition exhibits excellent numerical stability (no pivot selection required) and minimal storage requirements (only the lower triangular part of $\mathbf{L}$ needs to be stored), making it well-suited for the precomputation step of the ADMM algorithm.

The computation process of Cholesky decomposition is based on the following recursive relations. For the (i, j)-th element M_{ij} of matrix $\mathbf{M}$, the elements of the lower triangular matrix $\mathbf{L}$ are calculated as follows:

$$\begin{aligned} L_{ii} &= \sqrt{M_{ii} - \sum_{k=1}^{i-1}|L_{ik}|^2},\\ L_{ij} &= \frac{M_{ij} - \sum_{k=1}^{j-1} L_{ik}L_{jk}^*}{L_{jj}} \quad i > j \end{aligned}\tag{13}$$

The total computational cost of this process was $\frac{1}{3}N^3 + \mathcal{O}(N^2)$ floating-point operations (FLOPs), corresponding to the time complexity of $\mathcal{O}(N^3)$. Although the decomposition itself still has a cubic complexity, it is a one-time precomputation cost. Once Cholesky decomposition $\mathbf{L}$ is obtained, solving the linear system $\mathbf{Mx} = \mathbf{b}$ is transformed into solving two triangular systems. First, intermediate vector $\mathbf{y}$ is obtained by solving $\mathbf{Ly} = \mathbf{b}$ via forward substitution.

$$y_i = \frac{b_i - \sum_{j=1}^{i-1} L_{ij} y_j}{L_{ii}}, \quad i = 1, 2, \ldots, N \tag{14}$$

Then, the final solution $\mathbf{x}$ is obtained by solving $\mathbf{L}^H \mathbf{x} = \mathbf{y}$ via backward substitution:

$$x_i = \frac{y_i - \sum_{j=i+1}^{N} L_{ji}^* x_j}{L_{ii}}, \quad i = N, N-1, \ldots, 1 \tag{15}$$

Each triangular system solution required N^2 floating-point operations (FLOPs), resulting in a total solution cost of $2N^2 + \mathcal{O}(N) = \mathcal{O}(N^2)$. In this manner, we reduce the complexity of solving the linear system in each iteration from $\mathcal{O}(N^3)$ to $\mathcal{O}(N^2)$, achieving an order-of-magnitude performance improvement.

From the perspective of overall computational complexity, assuming that the ADMM algorithm requires K iterations to converge, the total computational cost with the precomputation strategy is $\mathcal{O}(N^3) + K \cdot \mathcal{O}(N^2) = \mathcal{O}(N^3 + KN^2)$. In practical applications, $K \ll N$ generally holds (e.g., K ranges from tens to hundreds, whereas N may reach millions), so the total complexity is actually close to $\mathcal{O}(N^3)$. In contrast, the complexity of the original method without precomputation is $K \cdot \mathcal{O}(N^3) = \mathcal{O}(KN^3)$. The ratio of the two complexities is approximately K, which means that the precomputation strategy can improve performance by tens or even hundreds of times.

3.3. Dual Momentum Coupling Mechanism

To further reduce the required number of iterations, this paper proposes a Dual-Momentum Coupled Mechanism based on the standard Nesterov momentum acceleration, which includes a two-level momentum design, in which the dual variables $\mathbf{u}_1$ and $\mathbf{u}_2$ are complex-valued and can be expressed as:

$$\mathbf{u} = \mathbf{u}_\mathrm{r} + \mathrm{j}\mathbf{u}_\mathrm{i} \tag{16}$$

The traditional Nesterov momentum only performs extrapolation within each component:

$$\mathbf{u}_\mathrm{eff}^{(k)} = \mathbf{u}^{(k)} + \beta\left(\mathbf{u}^{(k)} - \mathbf{u}^{(k-1)}\right) \tag{17}$$

There was a strong correlation between the error evolution processes of the real and imaginary parts. Therefore, we introduce cross-momentum terms to update the real part affected by the variation trend of the imaginary part, and vice versa, where the effective dual variable update is defined as:

$$\mathbf{u}_\mathrm{r}^\mathrm{eff} = \mathbf{u}_\mathrm{r}^{(k)} + \beta\left(\mathbf{u}_\mathrm{r}^{(k)} - \mathbf{u}_\mathrm{r}^{(k-1)}\right) + \gamma\left(\mathbf{u}_\mathrm{i}^{(k)} - \mathbf{u}_\mathrm{i}^{(k-1)}\right) \tag{18}$$

$$\mathbf{u}_\mathrm{i}^\mathrm{eff} = \mathbf{u}_\mathrm{i}^{(k)} + \beta\left(\mathbf{u}_\mathrm{i}^{(k)} - \mathbf{u}_\mathrm{i}^{(k-1)}\right) + \gamma\left(\mathbf{u}_\mathrm{r}^{(k)} - \mathbf{u}_\mathrm{r}^{(k-1)}\right) \tag{19}$$

The value ranges of the primary momentum coefficient β and the coupling strength parameter γ are jointly defined by the algorithm stability and the momentum coupling mechanism. Specifically, as a first-order momentum coefficient, β is restricted to the range of $(0, 1)$ to ensure the stability of inertial acceleration. In contrast, γ, which is used to introduce momentum interaction between the real and imaginary components, is limited to the interval $[0, \beta)$; this ensures that the coupled momentum always serves as a supplement to the primary inertial term, thereby avoiding numerical instability caused by excessive momentum superposition.

In addition to dual-side acceleration, this study further introduces a primal momentum term into the right-hand side (RHS) of the $\mathbf{x}$-update to form a composite acceleration structure. Let $\mathbf{x}^{(k-1)}$ and $\mathbf{x}^{(k-2)}$ be the primal variables of the previous two iterations. Then, the momentum increment is defined as:

$$\Delta\mathbf{X}_\mathrm{mom} = \alpha\left(\mathbf{x}^{(k-1)} - \mathbf{x}^{(k-2)}\right) \tag{20}$$

It is added as an "inertial push" to the right-hand side vector of the $\mathbf{x}$-update as follows:

$$\mathbf{b}^k \leftarrow \mathbf{b}^k + \Delta\mathbf{x}_\mathrm{mom} \tag{21}$$

where $\alpha \in [0, \beta)$ is a momentum weighting parameter that scales the inertial contribution in the update rule. The lower bound $\alpha = 0$ corresponds to disabling the additional inertial weighting, while the upper bound $\alpha < \beta$ ensures that the weighted inertial term remains subordinate to the primary momentum coefficient. This constraint prevents excessive accumulation of inertia and contributes to the numerical stability of the iterative process.

In summary, the complete momentum mechanism process is as follows. If $k > 1$, calculate the effective dual variables $\mathbf{u}_\mathrm{r}^\mathrm{eff}$ and $\mathbf{u}_\mathrm{i}^\mathrm{eff}$ based on historical values; construct the right-hand side term $\mathbf{b}^k$ with primal momentum, quickly solve $\mathbf{x}^{k+1}$ using Cholesky decomposition, update all variables, and record the current state for subsequent use.

The two components jointly form an efficient acceleration loop: the precomputation strategy based on Cholesky decomposition significantly reduces the solution overhead of the $\mathbf{x}$-update; the novel dual-momentum coupling mechanism, based on Nesterov extrapolation, introduces momentum interaction between the real and imaginary parts of dual variables and integrates the historical variation trend of the primal variables, further accelerating the overall convergence speed.

4. EXPERIMENTS AND RESULTS ANALYSIS

4.1. Simulated Data

This section presents a simulation analysis of point targets in the squint imaging mode of an airborne strip-map SAR system. The simulation experiments obtained imaging results and performed performance analysis on the Range-Doppler (RD) algorithm, L_1-regularization algorithm [5], L_1&TV-regularization algorithm [10], ADMM algorithm [16], and the algorithm proposed in this paper. The simulation parameters are listed in Table 1. First, the simulation imaging of 4-point targets is used

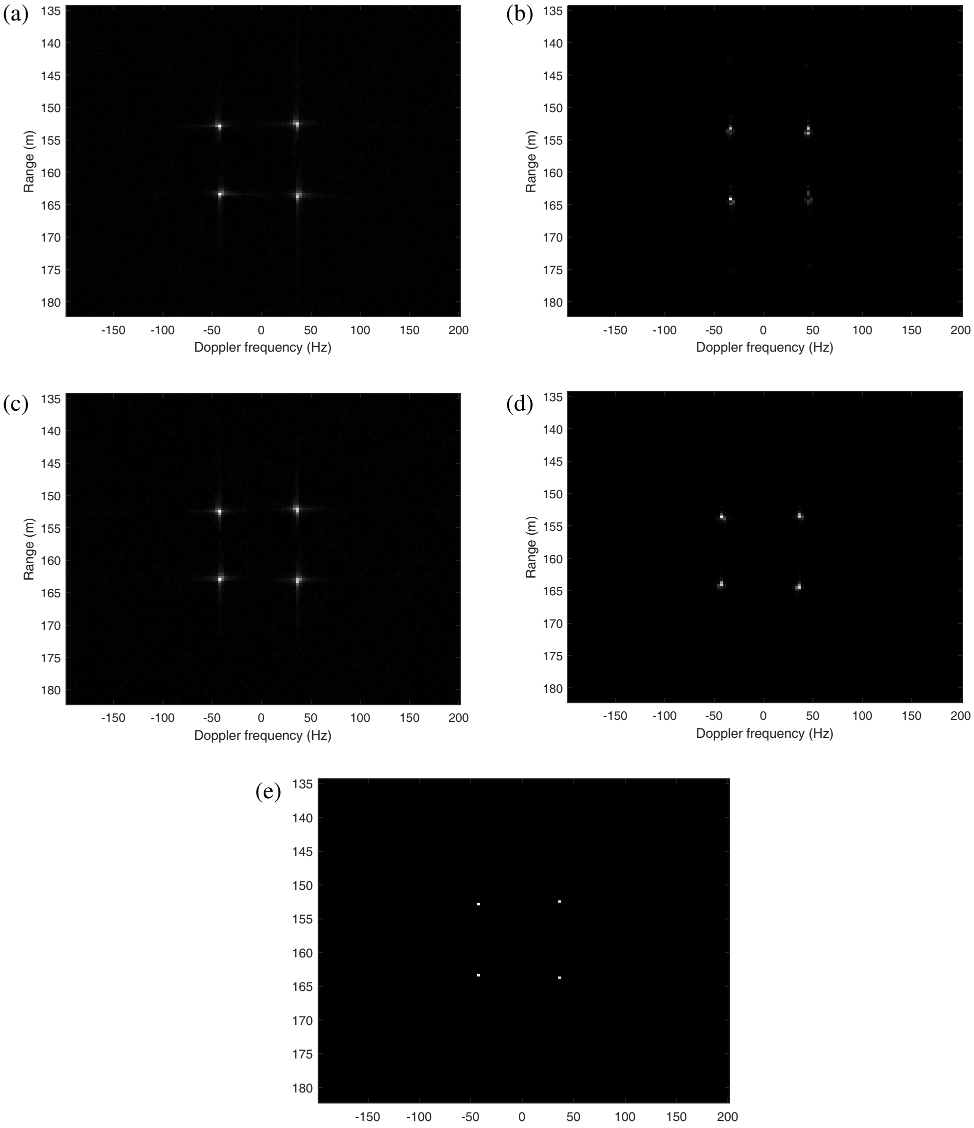

FIGURE 1. Point target simulation imaging results. (a) RD algorithm. (b) L_1-regularization algorithm. (c) L_1 & TV-regularization algorithm. (d) ADMM algorithm. (e) Proposed algorithm.

TABLE 1. Two-dimensional radar system parameters.

Parameter	Value
Radar Carrier Frequency (GHz)	10
Platform Velocity (m/s)	7
Radar Platform Altitude (m)	50
Signal-to-Noise Ratio (SNR)	10
Sampling Rate (MHz)	5

in order to verify the performance of the proposed algorithm. The imaging results of the five algorithms are shown in Fig. 1, where the two point targets in the first row are strong targets and the two-point targets in the second row are weak targets.

Point target simulation results of the RD algorithm are shown in Fig. 1(a). It can be observed that the RD algorithm can achieve point target imaging but exhibits strong sidelobes. For the point target imaging using regularization algorithms in Fig. 1(b) and Fig. 1(c), the sidelobes are suppressed, and the point target imaging is clearer than that of the RD algorithm, but scattering artifacts still exist. Specifically, the weak targets are also suppressed in Fig. 1(b) owing to the use of the L_1-regularization algorithm. The ADMM algorithm used in Fig. 1(d) was slightly inferior to the proposed algorithm, with relatively blurred imaging results. In contrast, the proposed algorithm, shown in Fig. 1(e), can achieve clear imaging of weak targets.

To evaluate the performance of each algorithm in imaging more intuitively, a profile analysis was performed by selecting the rows and columns with the strongest energy from the imaging results of each algorithm.

The experimental results in Fig. 2 indicate that the proposed algorithm exhibits a sharper main-lobe structure and a lower noise floor, demonstrating its excellent target focusing capability and anti-noise performance. The reconstruction quality was optimal for both the range and azimuth dimensions. In contrast,

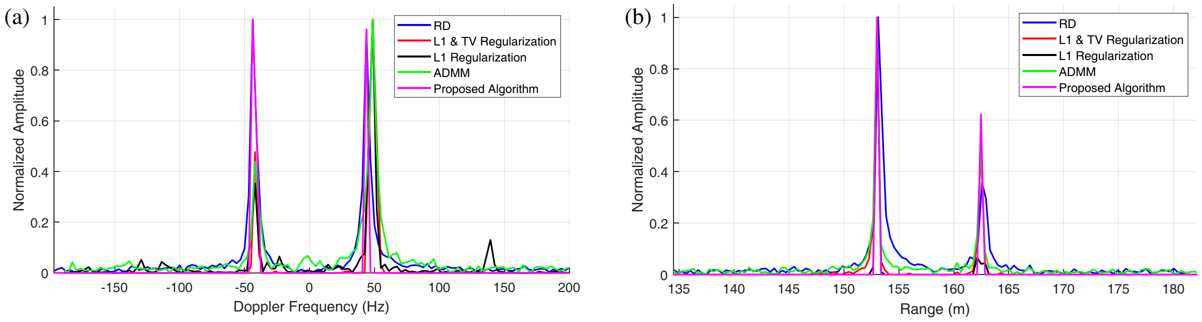

FIGURE 2. Imaging profiles. (a) Azimuth profile. (b) Range profile.

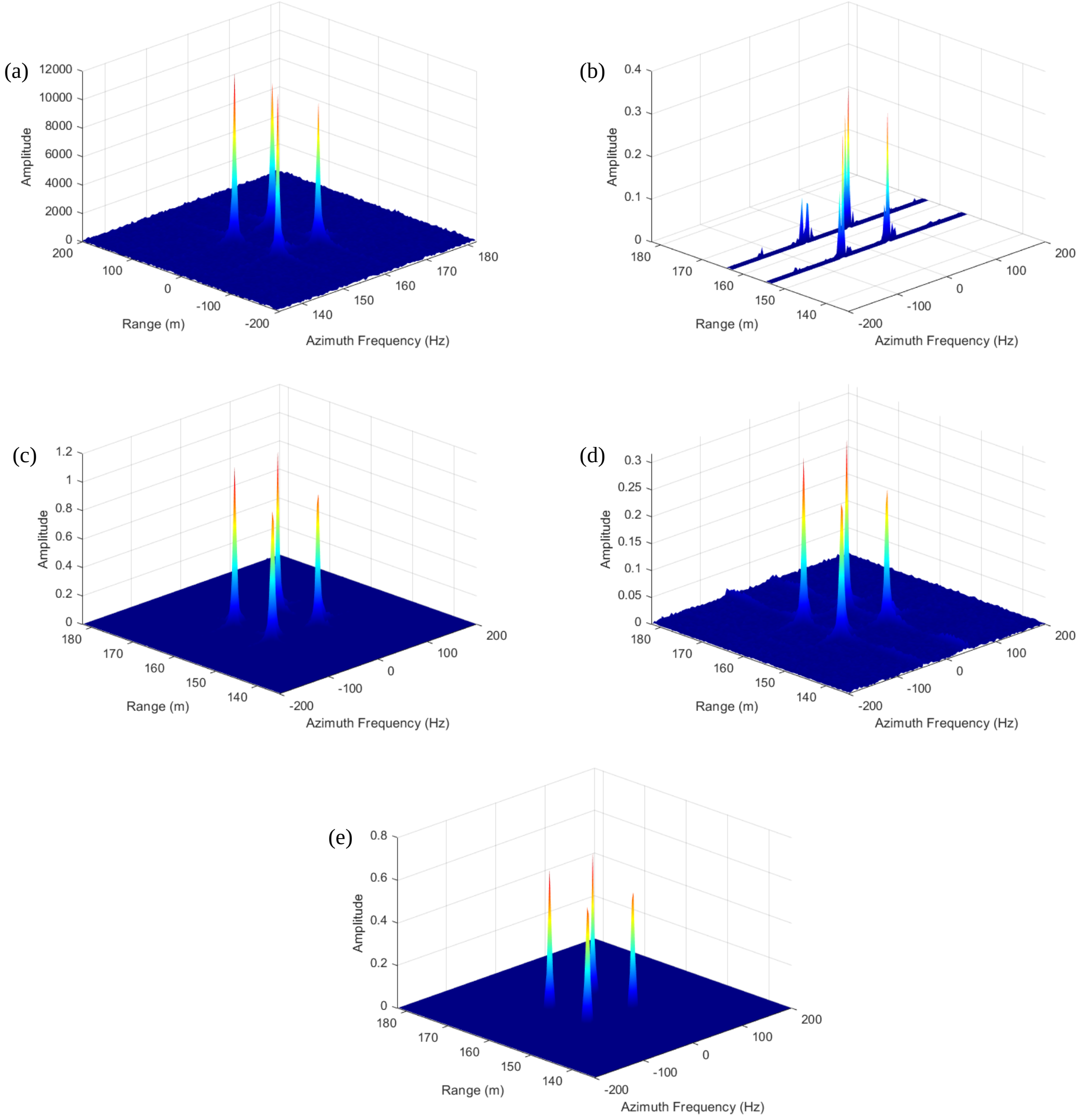

FIGURE 3. 3D visualization results. (a) RD algorithm. (b) L_1-regularization algorithm. (c) L_1 & TV-regularization algorithm. (d) ADMM algorithm. (e) Proposed algorithm.

other algorithms perform poorly in terms of anti-noise capability, with wider main lobes, limited image focusing effects, and noticeable noise artifacts. In particular, the L_1-regularization algorithm showed strong suppression of targets, resulting in an insufficiently prominent main lobe.

The 3D visualization results of the point target imaging for all algorithms are displayed in Fig. 3, which provides a comprehensive view of the energy distribution in the range, azimuth, and amplitude dimensions.

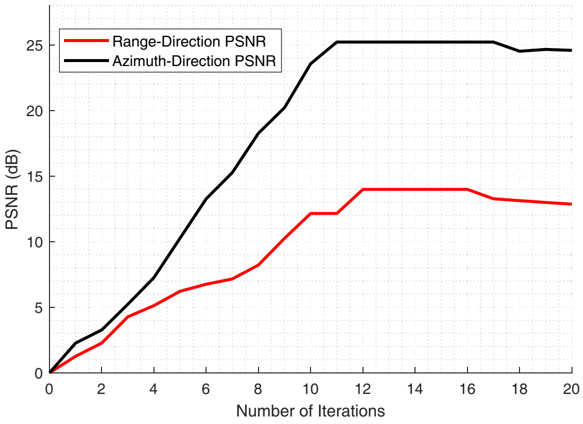

FIGURE 4. Influence of iteration times on PSNR.

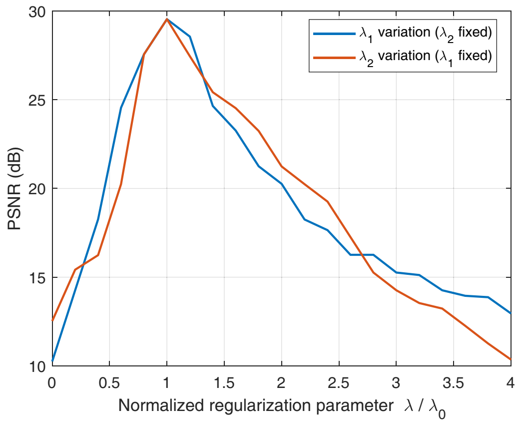

FIGURE 5. PSNR sensitivity to normalized λ.

Figure 3(a) presents the RD algorithm, which is a pure frequency-domain processing method that directly performs a two-dimensional Fast Fourier Transform on the de-skewed signal. Without any regularization constraints, the signal energy accumulates directly in the frequency domain, thus achieving extremely high-amplitude values. For the L_1-regularization algorithm in Fig. 3(b), excessive signal suppression results in blank areas at the bottom of the 3D image. Although the L_1 & Total Variation (TV)-regularization algorithm in Fig. 3(c) can suppress noise, its target focusing performance is inferior to that of the proposed algorithm. The ADMM algorithm in Fig. 3(d) failed to effectively suppress noise. By contrast, the proposed algorithm in Fig. 3(e) exhibits optimal performance in both imaging focusing and noise suppression.

To comprehensively evaluate the imaging performance of the proposed self-iterative algorithm under different values of three key metrics, namely, Peak Sidelobe Ratio (PSLR), Integrated Sidelobe Ratio (ISLR), and Impulse Response Width (IRW), the three key metrics are calculated for the point target imaging results of the aforementioned five algorithms. The results are summarized in Table 2.

TABLE 2. Performance comparison of different algorithms.

Algorithm	PSLR/dB	ISLR/dB	IRW/m
RD algorithm	-13.254	-10.262	1.667
L_1-regularization algorithm	-12.215	-12.215	1.640
L_1&TV-regularization	-14.626	-11.265	1.642
ADMM algorithm	-18.264	-15.265	1.765
Proposed Algorithm	-29.545	-30.262	1.641

As can be observed from Table 2, compared with the RD algorithm, the sparse SAR imaging algorithms (including the L_1-regularization algorithm, L_1 & TV-regularization algorithm, ADMM algorithm, and the proposed algorithm) exhibit a significantly improved Peak PSLR and ISLR. Meanwhile, the IRW was reduced, indicating an enhanced imaging resolution. Specifically, in comparison with the ADMM algorithm, the proposed algorithm achieves a remarkably higher PSLR and ISLR, along with a reduced IRW, which effectively improves the imaging resolution and facilitates the imaging of weak targets.

In addition, the algorithm proposed in this study requires iterative updates of each variable, and the number of iterations has a certain impact on the imaging accuracy. Taking the PSNR as an example, the influence of the number of iterations on the PSNR is illustrated in Fig. 4. The proposed algorithm achieved optimal performance at approximately the 12th iteration. With a further increase in the number of iterations, the PSNR remained stable at a constant value. However, when the number of iterations continued to increase excessively, the PSNR gradually decreased. This phenomenon, commonly referred to as semi-convergence in iterative reconstruction algorithms, arises because the model begins to overfit the noise component in the measurement data rather than the true target signal, leading to a slight degradation in imaging quality. Overall, the proposed algorithm can achieve the maximum PSNR with a very small number of iterations, ensuring excellent reconstruction accuracy, while achieving fast convergence.

The fixed values of the key regularization parameters λ_1 and λ_2 in the proposed model are determined through controlled variable experiments. Specifically, a series of univariate control experiments are conducted to traverse the value ranges of λ_1 and λ_2, and the Peak Signal-to-Noise Ratio (PSNR) of the imaging results under different parameter combinations is calculated. Ultimately, $\lambda_1 = 0.1$ and $\lambda_2 = 0.01$, which maximize the PSNR, are selected as the fixed experimental values.

To intuitively demonstrate the rationality of the fixed values and parameter sensitivity, λ_1 and λ_2 are normalized by their respective optimal fixed values, and the curves of PSNR versus normalized regularization parameters are plotted Fig. 5. Specifically, the blue curve illustrates the variation of PSNR with the normalized λ_1 when $\lambda_2 = 0.01$ (experimentally determined optimal value) is fixed; the red curve depicts the variation of PSNR with the normalized λ_2 when $\lambda_1 = 0.1$ (experimentally determined optimal value) is fixed. The curve results show that PSNR reaches a peak of 29.54 dB centered at the experimentally determined fixed values (normalized value = 1), and any deviation from these values leads to a significant degradation in imaging quality. This verifies the optimality and rationality of the fixed parameter values.

FIGURE 6. Imaging results of the RADARSAT-1 measured data.

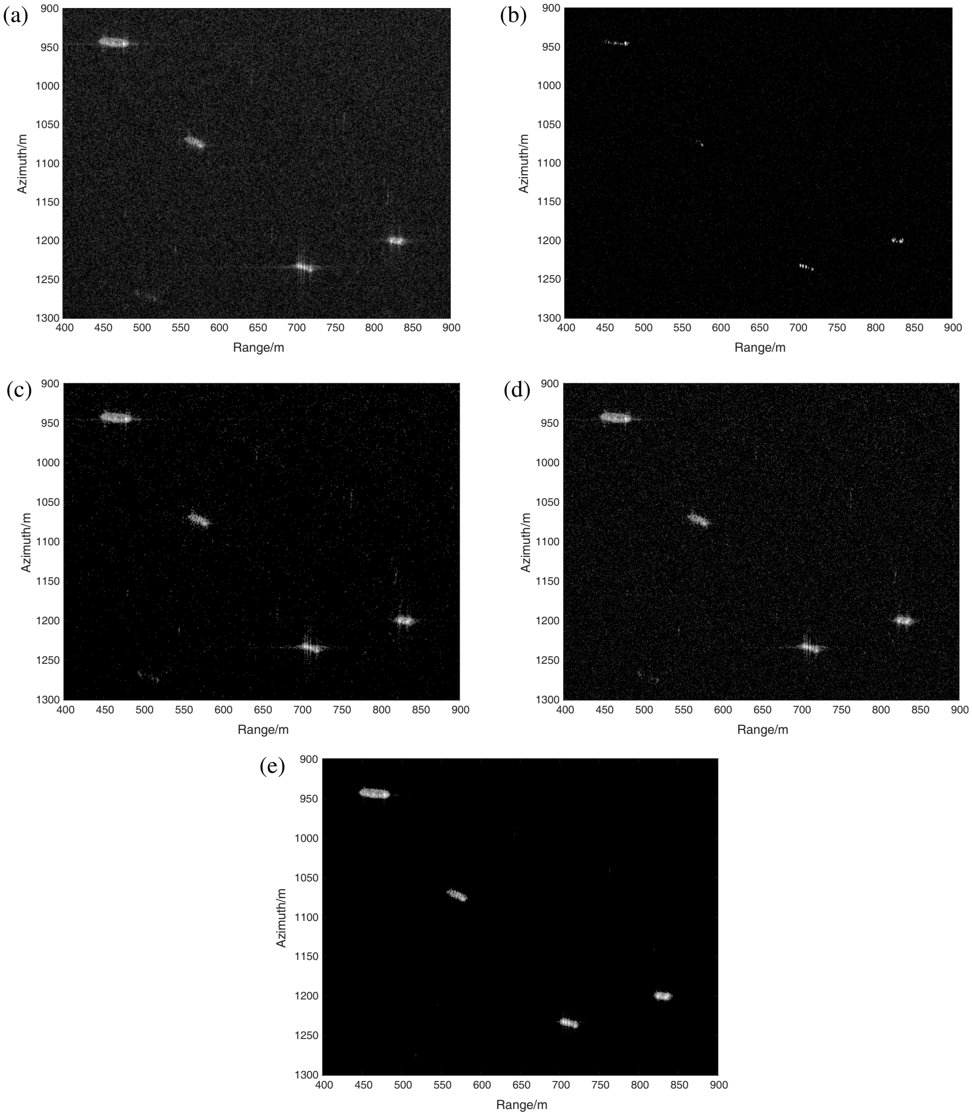

FIGURE 7. Imaging with real data. (a) RD algorithm. (b) L_1-regularization algorithm. (c) L_1 & TV-regularization. (d) ADMM algorithm. (e) Proposed algorithm.

4.2. Real Data

To fully verify the effectiveness of the algorithm proposed in this paper, measured data from RADARSAT-1 were adopted for experiments, with the imaging parameters summarized in Table 3. The imaging results of ships on the sea surface in the Vancouver, Canada area are presented in Fig. 6. For a better comparison of the imaging results, four ships within the red rectangular boxes were selected as research objects.

TABLE 3. Two-dimensional radar system parameters.

Parameter	Value
Radar Operating Frequency (GHz)	5.3
Pulse Width (MHz)	30.111
Radar Wavelength (m)	0.0566
Radar Velocity (m/s)	7062
Range Chirp Rate (MHz/s)	721350
Azimuth Chirp Rate (Hz/s)	1733
Range Sampling Rate (MHz)	3.2317
Pulse Repetition Frequency (Hz)	1257

The imaging results of the five algorithms are shown in Fig. 7. Fig. 7(a) presents the measured data imaging result of the RD algorithm, where a large amount of noise exists in the imaging of the ship targets. Fig. 7(b) shows the imaging result of the L_1-regularization algorithm; it can be observed that the noise is significantly reduced, but some weak targets on the ship are also suppressed. Fig. 7(c) and Fig. 7(d) depict the imaging results for the L_1 & TV-regularization algorithm and the ADMM algorithm, respectively. In these two results, the noise was clearly reduced, but the target intensity was also suppressed. Fig. 7(e) shows the measured data imaging result of the proposed algorithm. Compared with other algorithms, it not only achieves a better noise suppression effect but also enhances the scattering intensity of ship targets, demonstrating certain advantages in practical scenario imaging.

From the aforementioned experimental results and analysis, it can be concluded that the proposed algorithm exhibits excellent imaging performance in practical scenarios. It can effectively suppress scene noise and sidelobes, thus possessing a considerable practical application value.

5. CONCLUSION

This study addresses the computational complexity and storage challenges faced by high-resolution Synthetic Aperture Radar (SAR) imaging, focusing on the efficiency optimization of sparse reconstruction in the complex domain. A compressed sensing imaging scheme based on hyperparameter self-iteration is proposed, and key research conclusions are derived through theoretical analysis and experimental verification.

To address the solution challenge of the combined L_1-TV regularization composite model, the Alternating Direction Method of Multipliers (ADMM) can decompose complex optimization problems into solvable subproblems. However, the solution of large-scale linear systems during the primal variable update phase remains a core bottleneck that restricts the efficiency. By leveraging the Hermitian positive definite property of the coefficient matrix, this study introduces Cholesky decomposition during the algorithm initialization phase and implements a "one-time decomposition, multiple reuses" strategy. This successfully reduces the computational complexity of solving the linear system in each iteration from $O(N^3)$ to $O(N^2)$, significantly lowering the computational overhead and laying a crucial foundation for improving the real-time performance of the algorithm.

Meanwhile, to further reduce the number of iterations required for convergence, the proposed dual-momentum coupling mechanism overcomes the limitation of traditional Nesterov momentum, which only performs extrapolation within a single component. By constructing a cross-momentum interaction structure between the real and imaginary parts of the dual variables and integrating the historical variation trend of the primal variables to form a composite acceleration mode, the overall convergence speed of the algorithm is effectively accelerated, achieving a secondary improvement in computational efficiency.

The simulation experimental results demonstrate that the proposed algorithm exhibits a sharper main-lobe structure and a lower noise floor in point target imaging, with significantly superior weak target reconstruction performance compared with the RD, L_1-regularization, L_1 & TV regularization, and traditional ADMM algorithms. Furthermore, verification using RADARSAT-1 measured data confirms that the algorithm can not only effectively suppress background noise but also enhance target scattering intensity in ship target imaging scenarios, successfully achieving collaborative optimization of imaging accuracy and computational efficiency.

In summary, the proposed ADMM acceleration framework provides an efficient numerical solution for sparse imaging in the complex domain. Its core ideas can be further extended to other complex domain signal processing fields such as MRI. In the future, the robustness and generalization ability of the algorithm in complex scenarios can be further improved by exploring adaptive hyperparameter adjustment strategies, thereby providing technical support for more high-resolution imaging tasks.

ACKNOWLEDGEMENT

This document is the result of the research project funded by the National Natural Science Foundation of China, Projects: Study on the process of snow melting of glacier debris disaster in the kilometer-level valley — taking the Duku Highway as an example with the project number 42372325.

REFERENCES

[1] Li, C., Z. Yu, and J. Chen, "Overview of techniques for improving high-resolution spaceborne SAR imaging and image quality," *Journal of Radars*, Vol. 8, No. 06, 717–731, 2019.

[2] Deng, Y., W. Yu, P. Wang, D. Xiao, W. Wang, K. Liu, and H. Zhang, "The high-resolution synthetic aperture radar system and signal processing techniques: Current progress and future prospects," *IEEE Geoscience and Remote Sensing Magazine*,

Vol. 12, No. 4, 169–189, 2024.

[3] Wang, T., B. Liu, Q. Wei, K. Kang, Q. Yu, and B. Cong, "A review on research progresses of compressed sensing imaging radar," *Electronics Optics & Control*, Vol. 26, No. 7, 1–8, 2019.

[4] Bi, H., B. Zhang, X. X. Zhu, W. Hong, J. Sun, and Y. Wu, "L_1-regularization-based sar imaging and CFAR detection via complex approximated message passing," *IEEE Transactions on Geoscience and Remote Sensing*, Vol. 55, No. 6, 3426–3440, 2017.

[5] Wu, C., H. Bi, B. Zhang, Y. Lin, and W. Hong, "L_1 regularization recovered SAR images based interferometric SAR imaging via complex approximated message passing," in *Image and Signal Processing for Remote Sensing XXIII*, Vol. 10427, 347–356, Warsaw, Poland, 2017.

[6] Bi, H., Y. Li, D. Zhu, G. Bi, B. Zhang, W. Hong, and Y. Wu, "An improved iterative thresholding algorithm for L_1-norm regularization based sparse SAR imaging," *Science China Information Sciences*, Vol. 63, No. 11, 219301, 2020.

[7] Yuan, T., Y. Wang, H. Kuang, Z. Wang, and Z. Ding, "Multipath ghost suppression of extended targets based on SAR parametric sparse imaging model," *Journal of Signal Processing*, No. 9, 1596–1607, 2023.

[8] Zeng, J., S. Lin, Y. Wang, and Z. Xu, "$L_{1/2}$ regularization: Convergence of iterative half thresholding algorithm," *IEEE Transactions on Signal Processing*, Vol. 62, No. 9, 2317–2329, 2014.

[9] Güven, H. E., A. Güngör, and M. Çetin, "An augmented Lagrangian method for complex-valued compressed SAR imaging," *IEEE Transactions on Computational Imaging*, Vol. 2, No. 3, 235–250, 2016.

[10] Liu, M., Z. Xu, T. Chen, B. Zhang, and Y. Wu, "Low oversampling staggered SAR imaging method based on L_1 & TV regularization," *Systems Engineering and Electronics*, Vol. 45, No. 9, 2718–2726, 2023.

[11] Xu, Z., M. Liu, G. Zhou, Z. Wei, B. Zhang, and Y. Wu, "An accurate sparse SAR imaging method for enhancing region-based features via nonconvex and TV regularization," *IEEE Journal of Selected Topics in Applied Earth Observations and Remote Sensing*, Vol. 14, 350–363, 2020.

[12] Diao, H., Y. Geng, and R. Tang, "Non-radiating elastic sources in inhomogeneous elastic media at corners with applications," *ArXiv Preprint ArXiv:2502.14468*, 2025.

[13] Diao, H., H. Liu, and Q. Meng, "Dislocations with corners in an elastic body with applications to fault detection," *SIAM Journal on Applied Mathematics*, Vol. 85, No. 5, 2399–2424, 2025.

[14] Diao, H., H. Liu, Q. Meng, and L. Wang, "On a coupled-physics transmission eigenvalue problem and its spectral properties with applications," *Journal of Differential Equations*, Vol. 441, 113508, 2025.

[15] Zhou, W., H. Diao, and H. Liu, "Quasi-minnaert resonances in high-contrast acoustic structures and applications to invisibility cloaking," *Journal of Computational Physics*, Vol. 541, 114310, 2025.

[16] Boyd, S., N. Parikh, E. Chu, B. Peleato, and J. Eckstein, "Distributed optimization and statistical learning via the alternating direction method of multipliers," *Foundations and Trends® in Machine learning*, Vol. 3, No. 1, 1–122, 2011.

[17] Chen, H., X. Tian, and W. Wang, "Beampattern synthesis for conformal FDA-MIMO," *Journal of Signal Processing*, Vol. 39, No. 5, 793–806, 2023.

[18] Wang, W., Z. Shang, Z. Zhou, and H. Liu, "Joint convolutional analysis and synthesis sparse representation-based component substitution fusion method for remote sensing images," *Journal of Signal Processing*, Vol. 38, No. 3, 571–581, 2022.

[19] Song, P., S. Li, W. Zhang, W. Zheng, and L. Zhao, "Transfer discriminant regression for cross-domain speech emotion recognition," *Journal of Signal Processing*, Vol. 39, No. 4, 649–657, 2023.

[20] Zhang, Q., H. Zhang, J. Ni, and Y. Luo, "A survey of synthetic aperture radar imaging methods based on deep learning," *Journal of Signal Processing*, Vol. 39, No. 9, 1521–1551, 2023.

[21] Wen, C., Y. Huang, J. Wu, J. Peng, Y. Zhou, and J. Liu, "Cognitive antideception-jamming for airborne array radar via phase-only pattern notching with nested ADMM," *IEEE Access*, Vol. 7, 153 660–153 674, 2019.

[22] Zhu, X. and J. Lai, "Recursive sparse LU decomposition based on nested dissection and low rank approximations," *Journal of Computational Physics*, Vol. 539, 114231, 2025.

[23] Guo, L., R. W. Yeung, and X.-S. Gao, "Proving information inequalities by gaussian elimination," *IEEE Transactions on Information Theory*, Vol. 71, No. 4, 2315–2328, 2025.

[24] Dai, D., C. Hao, S. Jin, and Y. Liang, "Regularized estimation of kronecker structured covariance matrix using modified cholesky decomposition," *Journal of Statistical Computation and Simulation*, Vol. 95, No. 5, 905–930, 2025.